Electronic Supplementary Information

Oxygen-deficient $Li_2ZnTi_3O_8$ anode for high-performance lithium storage

Huanhuan Liu,[a] Xue Zhang,[a] Zhongxue Zhang,[a] Lijuan Wang,*[a] Zhaohui Meng *[b] and Zhiyuan Tang [c]

a College of Petroleum and Chemical Technology, Liaoning Petrochemical University, Fushun 113001, Liaoning, China

b College of Chemistry and Pharmaceutical Engineering, Nanyang Normal University, Nanyang, 473061, Henan, China

c Department of Applied Chemistry, School of Chemical Engineering and Technology, Tianjin University, Tianjin 300072, China

*Corresponding authors:

Mrs. Lijuan Wang

E-mail address: lijuanw123@163.com

Tel.: +8624-56861711

Mr. Zhaohui Meng

E-mail address: nysymengzhaohui@126.com

Table of Contents

I. Experimental

Materials synthesis

The preparation of the precursors for LZTO is the same as that in our previous work [1]. And then the precursors were calcined for 3 h at 700 ℃ in flowing N_2, air and O_2, with the flowing rates of 2.5, 1000 and 2.5 mL min^{-1} for N_2, air and O_2, respectively. The obtained samples were marked as LZTO-FN, LZTO-FA and LZTO-FO, respectively.

Physical and electrochemical characterizations

The phases and crystal structures were examined by X-ray diffraction (XRD) on a Bruker D8 Advance X-ray diffractometer (Cu Kα radiation, λ = 1.54 Å) in the 2θ range of 10-85 °. The morphologies were inspected via a SU8010 scanning electron microscope (SEM). The nanoscale microstructures were observed via a JEM-2100F high-resolution transmission electron microscope (HR-TEM). The surface species were determined by X-ray photoelectron spectra (XPS) on a PHI 5600 CI X-ray photoelectron spectrometer using mono-chromatic Al-Ka radiation. The electronic conductivity was obtained from a four-probe system (SB100A/2). A JES-FA200 instrument was used to record the electronic paramagnetic resonance (EPR) spectroscopies of the samples. Raman spectroscopies were performed on a DXR Raman spectrometer with a laser excitation wavelength of 512 nm. The specific surface areas and pore size distributions were measured by a 3H-2000PS2 specific surface area and pore size distribution analyzer via nitrogen adsorption. The surface compositions of the electrode were analyzed using a Fourier transform infrared

spectroscopy (FT-IR) spectrometer (Bruker VERTEX 70).

CR2025 coin-type cells were assembled to test the electrochemical performance. The working electrodes were obtained by pasting the slurry including 85 wt.% active material, 10 wt.% conductive agent, and 5 wt.% binder of polyvinylidene difluoride on a Cu foil. The assembly of the cells was carried out in a glove box filled with high purity Ar. For the half cells, $Li_2ZnTi_3O_8$ or $LiNi_{0.5}Mn_{1.5}O_4$ is used as the working electrode and the fresh lithium foil is used as the counter/reference electrode. The loading of the active material is *ca*. 2.5 mg cm^{-2}. For the full cells, $LiNi_{0.5}Mn_{1.5}O_4$ and LZTO-FA were used as the positive electrode and negative electrode, respectively. The loading of LZTO-FA is *ca*. 1.6 mg cm^{-2} in the full cells. The specific capacities of the full cells are calculated based on the mass of the anode active material. The electrolyte was 1.2 M $LiPF_6$ dissolved into a mixture of ethylene carbonate and ethyl methyl carbonate (*V*/*V* = 3:7). $LiNi_{0.5}Mn_{1.5}O_4$ was purchased from Shenzhen Biyuan Electronics Co., Ltd in the work. Charge-discharge and cyclic voltammetry (CV) were tested in 0.02-3.0 V for the LZTO/Li half cells, 3.5-4.95 V for the $LiNi_{0.5}Mn_{1.5}O_4$/Li half cells, and 2-4.55 V for the $LiNi_{0.5}Mn_{1.5}O_4$/LZTO-FA full cells. The scan rates of CV measurements were 0.2-2.0 and 0.1 mV s^{-1} for the LZTO/Li half cells and $LiNi_{0.5}Mn_{1.5}O_4$/LZTO-FA full cells, respectively. Electrochemical impedance spectroscopies (EIS) were recorded in 10 mHz-100 kHz with an *ac* voltage of 5 mV.

Computation details

The first-principles calculations were carried out based on the Vienna Ab-initio Simulation Package (VASP) with the projector augmented wave (PAW) method [2-5].

The Perdew-Burke-Ernzerhof (PBE) functional of generalized gradient approximation (GGA) was used to describe the exchange correlation term. All geometrical structures were fully optimized to its ground state with a cutoff energy of 400 eV [6-8]. The energy and forces are converged to 1×10^{-5} eV and 0.01 eV $Å^{-1}$, respectively. According to the method of reference [9], GGA+U was adopted to underestimate the band gap. The Li^{+} diffusion was using climbing image nudged elastic band (CI-NEB) method [10].

II. Supplementary Figures 1-12 and Tables 1-11

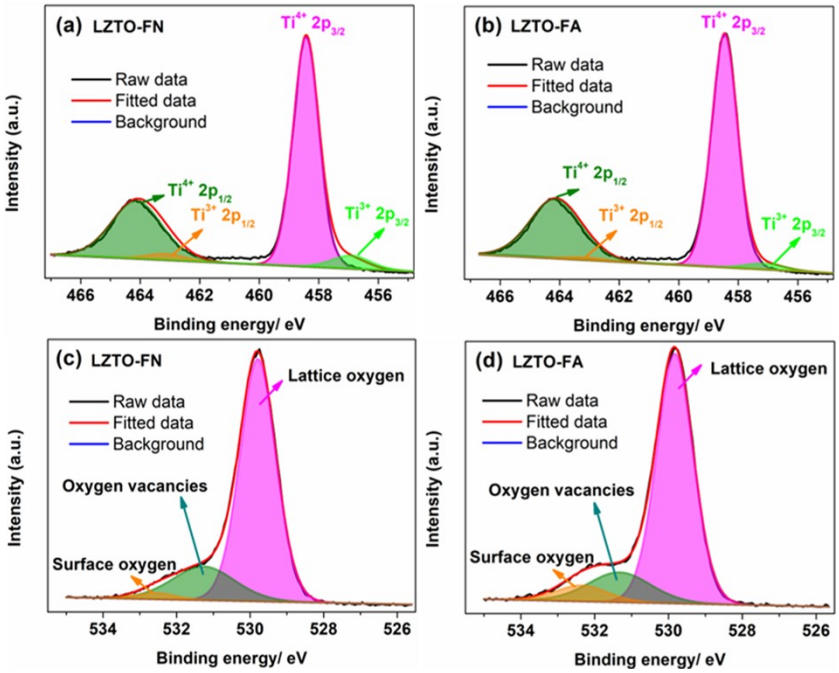

Fig. S1 High-resolution XPS spectra of (a-b) Ti 2p and (c-d) O 1s for LZTO-FN and LZTO-FA.

The high-resolution XPS spectra of Ti 2p and O 1s are shown in Fig. S1 for LZTO-FN and LZTO-FA. The peaks at 464.2 and 458.4 eV correspond to Ti $2p_{1/2}$ and Ti $2p_{3/2}$ [11], respectively. 457.1 and 463.2 eV are assigned to Ti^{3+} $2p_{3/2}$ and Ti^{3+} $2p_{1/2}$ [12], respectively. So, there are Ti^{3+} ions on the surfaces of LZTO-FN and LZTO-FA.

Moreover, the content of Ti^{3+} for LZTO-FN is higher than that of LZTO-FA. The presence of Ti^{3+} could be associated with the formation of oxygen vacancies after heat treatment [13]. For the O ls XPS spectra of LZTO-FN and LZTO-FA, peaks at 529.7, 531.1 and 532. 6 eV can be ascribed to the lattice oxygen species (O_L), oxygen vacancies (O_V) and the oxygen absorbed on the surfaces of the materials (O_S), respectively [13-15]. The percentage of OVs for LZTO-FN is higher than that of LZTO-FA (Table S1).

Table S1 Comparison of XPS results, and electronic conductivity for LZTO-FN and LZTO-FA.

Samples	XPS (%)		XPS (%)			σ (S cm^{-1})
	Ti^{4+}	Ti^{3+}	O_L	O_V	O_S	
LZTO-FN	92.21	7.79	78.79	19.03	2.18	1.70×10^{-5}
LZTO-FA	96.27	3.73	77.33	15.78	6.89	1.36×10^{-5}

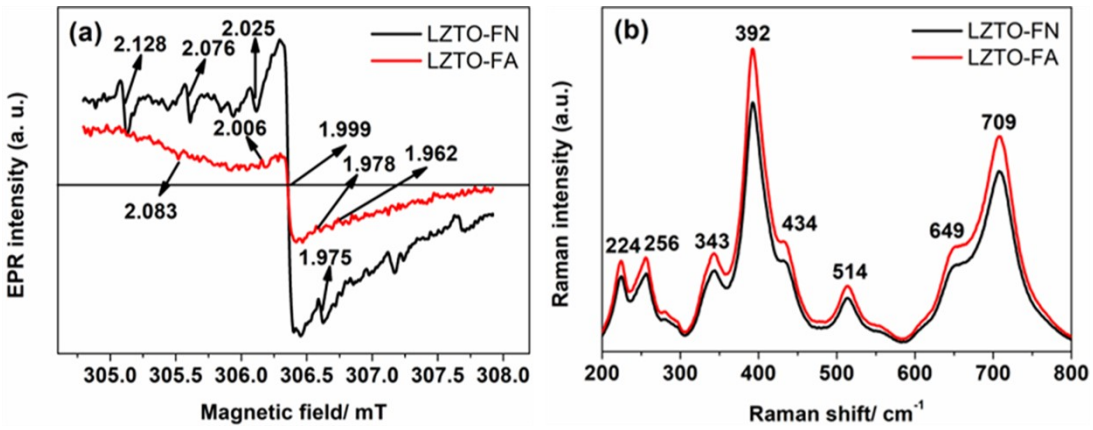

Fig. S2 (a) Electron paramagnetic resonance (EPR) spectra and (b) Raman spectra of LZTO-FN and LZTO-FA.

Electron paramagnetic resonance (EPR) is an effective tool to characterize the paramagnetic species such as Ti^{3+}, and defect structures [16]. The *g*-value of Ti^{3+} is 1.94-1.99 as reported in previous work [17]. The signal *ca*. g = 2.0 is attributed to OVs as reported [18]. So, both Ti^{3+} and OVs exist in LZTO-FN and LZTO-FA (Fig. S2a). In addition, the content of Ti^{3+} and OVs for LZTO-FN is higher than that of LZTO-FA.

The Raman spectroscopies of LZTO-FN and LZTO-FA are shown in Fig. S2b. The main peaks are at 224, 256, 343, 392, 434, 514, 649, and 709 cm^{-1} for LZTO. The strongest peak at 392 cm^{-1} can be assigned to A 1g mode of ZnO_4 tetrahedra. The band at 434 cm^{-1} corresponds to the stretching vibrations of the Li-O bonds in LiO_4 tetrahedra. The high frequency band at 709 cm^{-1} is assigned to the symmetric stretching vibrations of the Ti-O bonds in TiO_6 octahedral groups [19]. Compared with LZTO-FA, the band intensities decrease for LZTO-FN, indicating the increase of the Ti^{3+}/Ti^{4+} molar ratio and OVs in LZTO-FN [20].

Table S2 Lattice constants and cell volumes of LZTO-FN and LZTO-FA.

Samples	$a=b=c$ (Å)	V (Å^3)
LZTO-FN	8.364(1)	585.14
LZTO-FA	8.358(4)	583.96

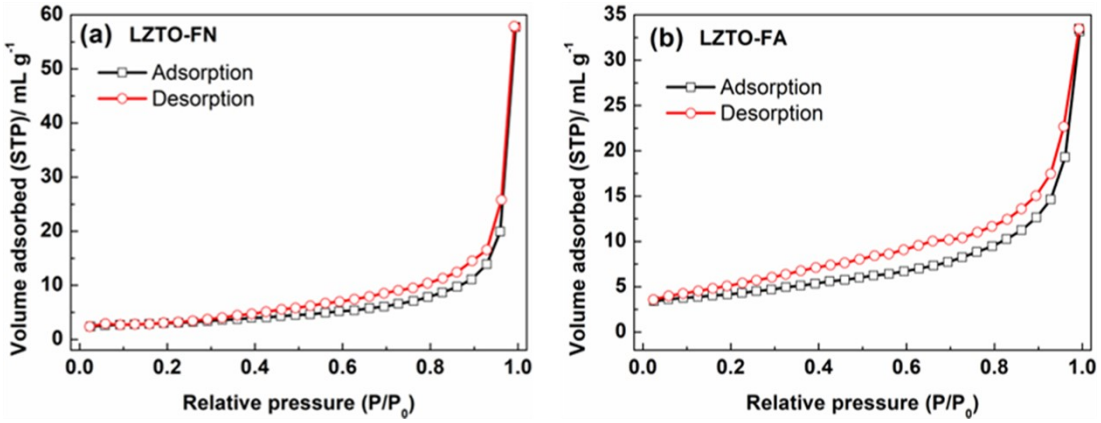

Fig. S3 N_2 adsorption-desorption isotherms of (a) LZTO-FN and (b) LZTO-FA.

Table S3 Specific surface areas, total pore volumes and pore diameters of LZTO-FN and LZTO-FA.

Samples	Specific surface areas (m^2 g^{-1})	Total pore volume (mL g^{-1})	Pore diameters (nm)
LZTO-FN	10.5	0.089	3.06
LZTO-FA	11.6	0.05	2.64

Table S4 Comparison of the CV peak potentials between LZTO-FN and LZTO-FA electrodes at the 1st cycle.

Samples	φ_{pa} (V)	φ_{pc} (V)	φ_p (V) = φ_{pa} - φ_{pc}
LZTO-FN	1.661	1.019	0.642
LZTO-FA	1.621	1.043	0.578

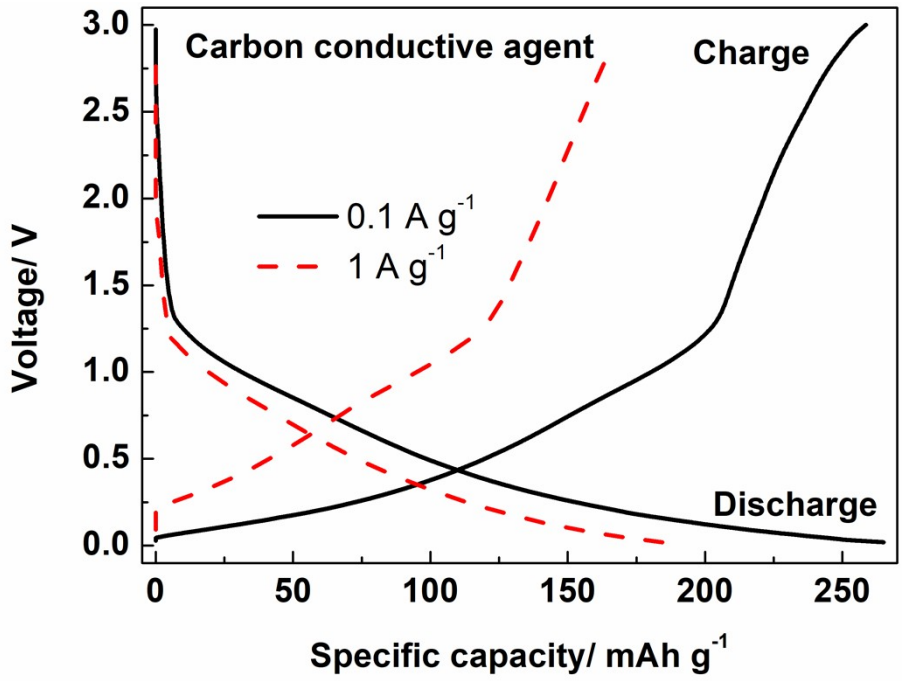

Fig. S4 Charge-discharge curves of the conductive agent at 0.1 and 1 A g^{-1}.

Table S5 Cycling performance of LZTO corresponding to the 2nd cycle in recent publications.

Materials	Current densities ($A\ g^{-1}$)	Cycle numbers	Capacity retention	References
LZTN3O	1	400	68.4%	[1]
$Li_2ZnTi_3O_8$@C	0.229	100	99.2%	[21]
$Li_2ZnTi_3O_8$@C	0.458	100	86.8%	[21]
LZTO-0	1	100	91.7%	[22]
LZTO-1	1	100	93.3%	[22]
LZTO-2	1	100	95.5%	[22]
LZTO-3	1	100	93.2%	[22]
LZTO	1	400	64%	[23]
$Li_2ZnTi_3O_8$@Li_2MoO_4	1	400	87%	[24]
$Li_2ZnTi_3O_8$@Li_2MoO_4	0.5/2	400	75.7%	[24]
LZTO-700-3	1	200	66.9%	[25]
LZTO@C-700-1	1	200	60.8%	[25]
LZTO@C-700-3	1	200	71.7%	[25]
LZTO@C-700-5	1	200	69.7%	[25]
LZTO-700-3	2	200	72.3%	[25]
LZTO@C-700-1	2	200	67.2%	[25]
LZTO@C-700-3	2	200	73.1%	[25]
LZTO@C-700-5	2	200	65.7%	[25]
LZTO@C-N-1	1	200	71.3%	[26]
LZTO@C-N-2	1	200	77.7%	[26]
LZTO@C-N-3	1	200	83.0%	[26]
LZTO@C-N-3	2	200	75.5%	[26]
LZTO	1	200	68.5%	[27]
LZTO@C-N-1	1	200	61.8%	[27]
LZTO@C-N-2	1	200	68.1%	[27]
LZTO@C-N-3	1	200	63.8%	[27]
LZTO@C-N-2	2	200	73.7%	[27]
LZTO@C-N-2	3	200	75%	[27]
LZTO	1	400	75.8%	[28]
LZTO/G	1	400	76.4%	[28]
LZTO	2	300	63.1%	[28]
LZTO/G	2	300	72.3%	[28]
LZTO@GNS	1	400	81.6%	[29]
LZTO@GNS-CNT	1	400	93.3%	[29]
LZTO@GNS	2	400	85.3%	[29]
LZTO@GNS-CNT	2	400	92.7%	[29]
LZTO	1	400	86.5%	[30]
LZTMO@G	1	400	87.2%	[30]
LZTO	2	300	57.2%	[30]
LZTMO@G	2	300	89.7%	[30]
LZTO@C	1	200	70.5%	[31]
LZTO@C	2	200	65.7%	[31]
LZTO@C@La_2O_3	1	200	89.8%	[31]

Table S5 (Contd.)

Materials	Current densities (A g^{-1})	Cycle numbers	Capacity retention	References
LZTO@C@La_2O_3	2	200	77.2%	[31]
LZTO-0	1.5	400	90%	[11]
LZTO-1	1.5	400	97.6%	[11]
LZTO/NMO	1	400	85.3%	[32]
LZTO/C-3	1	400	94.4%	[33]
LZTO	1	400	34.6%	[34]
LZTW3O	1	400	93.1%	[34]
LM6ZTW3O	1	400	94.7%	[34]
LZTO-FN	1	400	No decay	The work
LZTO-FA	2	400	No decay	The work

Table S6 Rate capability of LZTO in recent publications.

Materials	Current densities (A g^{-1})	Specific capacities (mAh g^{-1})	Cycle numbers	References
LZTO	2	78	25	[23]
$Li_2ZnTi_3O_8$@Li_2MoO_4	2	112	60	[24]
$Li_2ZnTi_3O_8$	2	55	60	[24]
LZTO-700-3	2.8	141.9	60	[25]
LZTO@C-700-1	2.8	174.5	60	[25]
LZTO@C-700-5	2.8	173.8	60	[25]
$Li_2ZnTi_3O_8$/TiO_2	2	173.4	50	[35]
$Li_2ZnTi_3O_8$/TiO_2	3	161.6	60	[35]
LZTO	1.145	47	106	[36]
LZTO@RGO10	1.145	50	106	[36]
LZTO@RGO25	1.145	154	106	[36]
LZTO@RGO50	1.145	113	106	[36]
LZTO-2	2.29	135	20	[37]
LZTNO	1.145	80	15	[38]
$Li_2ZnTi_3O_8$/C	2	178	60	[39]
LZTO/KCl	1.6	135.6	50	[40]
P-LZTO	1.6	53.3	40	[32]
LZTO/NMO	1.6	161.3	40	[32]
LZTO/NMO-1	1.6	101.8	40	[32]
P-LZTO	1.6	44	50	[41]
LZTO/LMS-1	1.6	107.1	50	[41]
LZTO/LMS-2	1.6	140.4	50	[41]
LZTO/LMS-3	1.6	144.9	50	[41]
PZ	1.6	69.3	50	[42]
FA1	1.6	124.5	50	[42]
FA2	1.6	144.3	50	[42]
FA3	1.6	96.1	50	[42]
FA2-800	1.6	143.5	50	[42]
FA2-850	1.6	127.6	50	[42]
P-LZTO	1.6	32.4	50	[43]
LZTO/LZO	1.6	109.8	50	[43]
LZTO/LZO-1	1.6	85.3	50	[43]
P-LZTO	1.6	65.8	50	[44]
LZTO/C-1	1.6	55.6	50	[44]
LZTO/C-2	1.6	106.7	50	[44]
LZTO/C-3	1.6	102.5	50	[44]
$Li_2ZnTi_{2.9}Cr_{0.1}O_8$	2	156.7	50	[45]
LZTO/C-3	2	169.8	40	[33]
LZTO/C-3	3	150.9	50	[33]
LZTO-E	2	138	40	[46]
LZTO-E	3	125	50	[46]
$Li_2Zn_{0.9}Nb_{0.1}Ti_3O_8$	2	160	40	[47]
$Li_2Zn_{0.9}Nb_{0.1}Ti_3O_8$	3	147	50	[47]
FLZTO-2	1	179.4	60	[48]
NWLZTO-2	1	132.8	60	[49]
LZTO-FA	1.5	192	60	The work

Table S6 (Contd.)

Materials	Current densities (A g^{-1})	Specific capacities (mAh g^{-1})	Cycle numbers	References
LZTO-FA	2	186.6	80	The work
LZTO-FA	2.5	180.7	100	The work
LZTO-FA	3	173.2	120	The work

Table S7 Rate capability of some other anodes with comparable theoretical specific capacity with LZTO in recent publications.

Materials	Current densities (A g^{-1}/C)	Specific capacities (mAh g^{-1})	Cycle numbers	References
N-doped TiO_2	2.5	150	80	[50]
TiO_2@CNT	5 C	122	40	[51]
TiO_2	5 C	116	50	[52]
TiO_2@C	5 C	90	30	[53]
TiO_2-carbonized PAN	1	74.7	40	[54]
$TiNb_2O_7$	1.6	145.7	50	[55]
$TiNb_2O_7$	6 C	183	35	[56]
$Ti_2Nb_{10}O_{29}$-CB-CO_2	2	100	35	[57]
A-$TiNb_2O_7$	10 C	174	50	[58]
m-$TiNb_2O_7$	10 C	157	55	[59]
$Ti_2Nb_{10}O_{29}$/AOSC	10 C	135.2	50	[60]
12% C-Nb_2O_5	10 C	137	30	[61]
M-Nb_2O_5	10 C	119	30	[62]
T-Nb_2O_5	10 C	117.3	30	[63]
A- Nb_2O_5	2	142	40	[64]
T-Nb_2O_{5-x}@NC-7	2	150	25	[65]
2D Nb2O5-C-rGO	10 C	175	40	[66]
Nb_2O_5@N-C	10 C	163	40	[67]
Li_3VO_4	2	110	25	[68]
Li_3VO_4	3	69	30	[68]
Li_3VO_4	0.2 C	168	10	[69]
LZTO-FA	2 (8.7 C)	186.6	80	The work
LZTO-FA	2.5 (10.9 C)	180.7	100	The work
LZTO-FA	3 (13.1 C)	173.2	120	The work

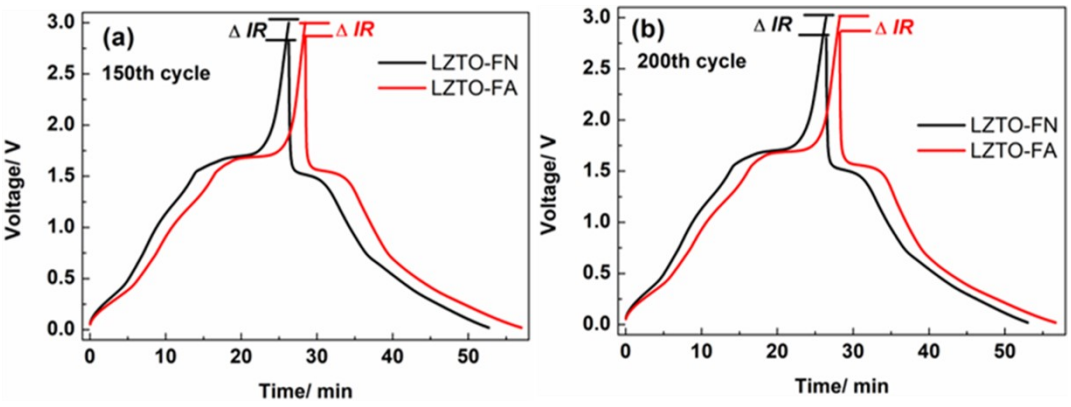

Fig. S5 *IR*-drop data of LZTO-FN and LZTO-FA electrodes at 0.5 A g^{-1} when charging is switched to discharging for the (a) 150th cycle and (b) 200th cycle.

The magnitude of internal resistance can be characterized by the voltage drop, or *IR* drop, when charging/discharging is switched to discharging/charging (Fig. S5). Compared with LZTO-FN, LZTO-FA has smaller *IR* drop during the cycling process.

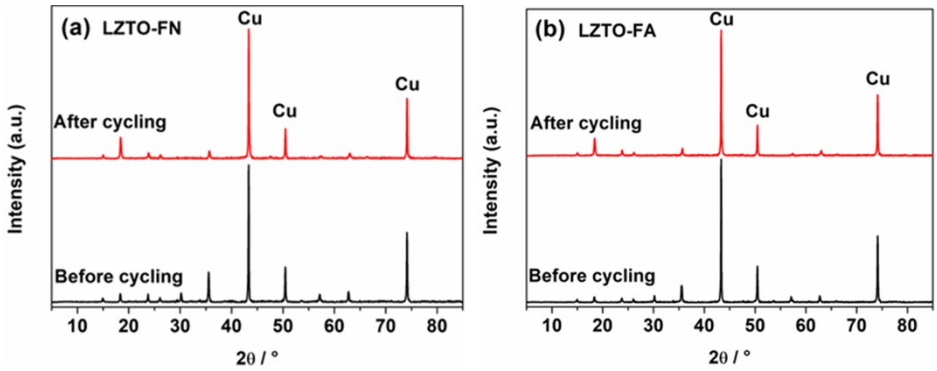

Fig. S6 Ex-situ XRD patterns of the LZTO-FN and LZTO-FA electrodes before and after cycling for 100 cycles at 1.5 A g^{-1} (55 ℃).

Table S8 Cell volumes of LZTO-FN and LZTO-FA electrodes before and after cycling at 1.5 A g^{-1} for 100 cycles (55 ℃).

Samples	Cell volumes ($Å^3$)	
	Before cycling	After cycling
LZTO-FN	586.6	585.0(8)
LZTO-FA	586.8(4)	587.3(8)

Fig. S6 presents the XRD patterns of the LZTO-FN and LZTO-FA electrodes before and after cycling for 100 cycles at 1.5 A g^{-1} (55 °C). It can be seen that some of the diffraction peaks of the LZTO-FN and LZTO-FA electrodes are blurry after cycling. The cell volume change ratios are 0.259% and 0.092% for LZTO-FN and LZTO-FA, respectively (Table S8), indicating that the structure of the LZTO-FA electrode with proper amount of OVs retains significantly stability during insertion and de-insertion of Li^+ ions. However, the structure of the LZTO-FN with excess OVs is partly changed during cycling process.

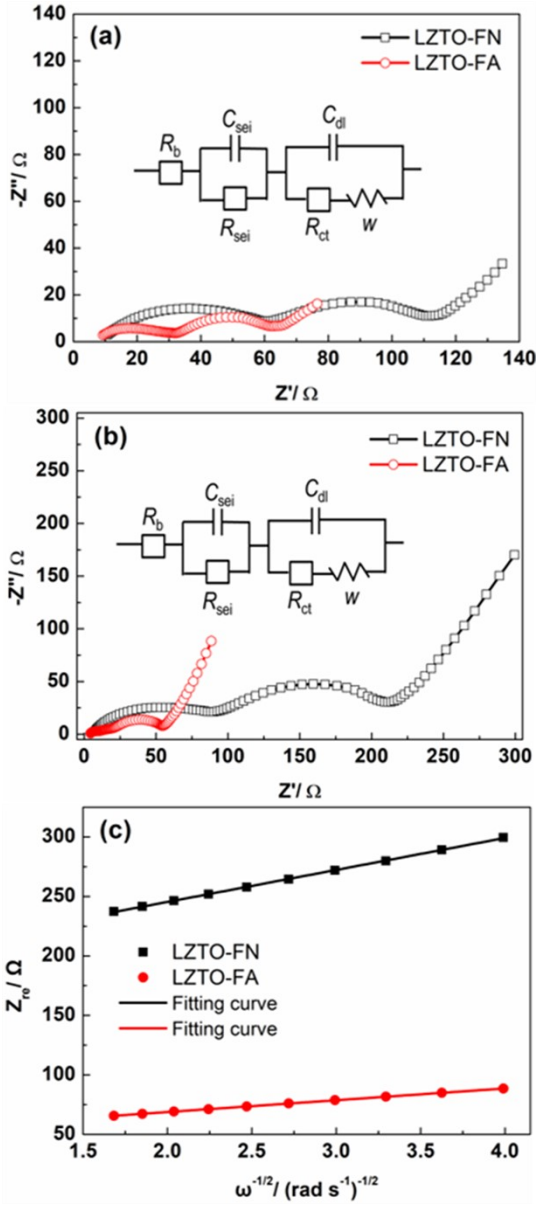

Fig. S7 Impedance spectra of the LZTO-FN and LZTO-FA electrodes (a) after cycling for 400 cycles at 2 A g^{-1}, and (b) after cycling at different current densities in Fig. 5d and corresponding equivalent circuits (inset). (c) Relationship between Z_{re} and $\omega^{-1/2}$.

Table S9 Impedance parameters calculated from equivalent circuit models, and lithium diffusion coefficients (D_{Li^+}) of LZTO-FN and LZTO-FA.

Samples	After 400 cycles			After 120 cycles			D_{Li+} ($cm^2\ s^{-1}$)
	R_b (Ω)	R_{sei}(Ω)	R_{ct} (Ω	R_b (Ω)	R_{sei} (Ω)	R_{ct} (Ω)	
LZTO-FN	13.95	40.4	42.23	10.32	65.9	95.09	6.6×10^{-11}
LZTO-FA	11.4	18.13	25.54	5.955	9.661	25.97	4.85×10^{-10}

EIS was tested on the cells cycling for 400 cycles at 2 A g^{-1} (Fig. S7a), and cycling at different current densities in Fig. 5d (Fig. S7b). For each curve, it is composed of a small intercept, two semicircles and a straight line. Figs. S7a-b (inset) are the equivalent circuit models. R_b represents the combined impedance between the electrolyte and cell components; C_{sei} and R_{sei} are the capacitance and the resistance of the SEI layer corresponding to the first semicircle; C_{dl} and R_{ct} are the double layer capacitance and charge transfer resistance corresponding to the second semicircle; W is Warburg impedance. Cycling for 400 cycles at 2 A g^{-1}, the R_{ct} is 40.4 and 18.13 Ω for LZTO-FN and LZTO-FA (Table S9), respectively. After cycling for several cycles at different current densities in Fig. 5d, the R_{ct} is 65.9 and 9.661 Ω for LZTO-FN and LZTO-FA (Table S9), respectively. It can be seen that LZTO-FA with proper amount of OVs has smaller R_{ct} than that of LZTO-FN with excess OVs. Small R_{ct} benefits for the electrochemical performance of LZTO-FA.

The diffusion coefficients of Li^+ ions (D_{Li^+}) in the two samples are estimated

based on the Warburg diffusion in low frequency (Fig. S7b) using the following equation [1]

$$D_{Li^+} = R^2T^2 / (2A^2n^4F^4C^2\sigma^2) \quad \text{(S1)}$$

where R is the gas constant (8.314 J mol^{-1} K^{-1}); T is the room absolute temperature (298.5 K); A is the surface area of the electrode (1.13 cm^2 in this work); n is the number of electrons transferred in the half reaction for the redox couple; F is Faraday constant (96,485 C mol^{-1}); C is the concentration of Li^+ ion in the compound, and can be calculated based on the following equation

$$C = \frac{3 \times 4}{6.022 \times 10^{23} \times V} \quad \text{(S2)}$$

σ is the Warburg factor which obeys the following relationship:

$$Z_{re} = R_e + R_{ct} + \sigma\omega^{-1/2} \quad \text{(S3)}$$

The relationship between Z_{re} and $\omega^{-1/2}$ is shown in Fig. S7c. Based on the Equations S1 and S3, D_{Li}^+ of LZTO-FN and LZTO-FA can be obtained and the values are 6.6×10^{-11} and 4.85×10^{-10} cm^2 s^{-1}, respectively. Compared with LZTO-FN electrode, LZTO-FA has higher D_{Li}^+, which is advantageous to its rate capability.

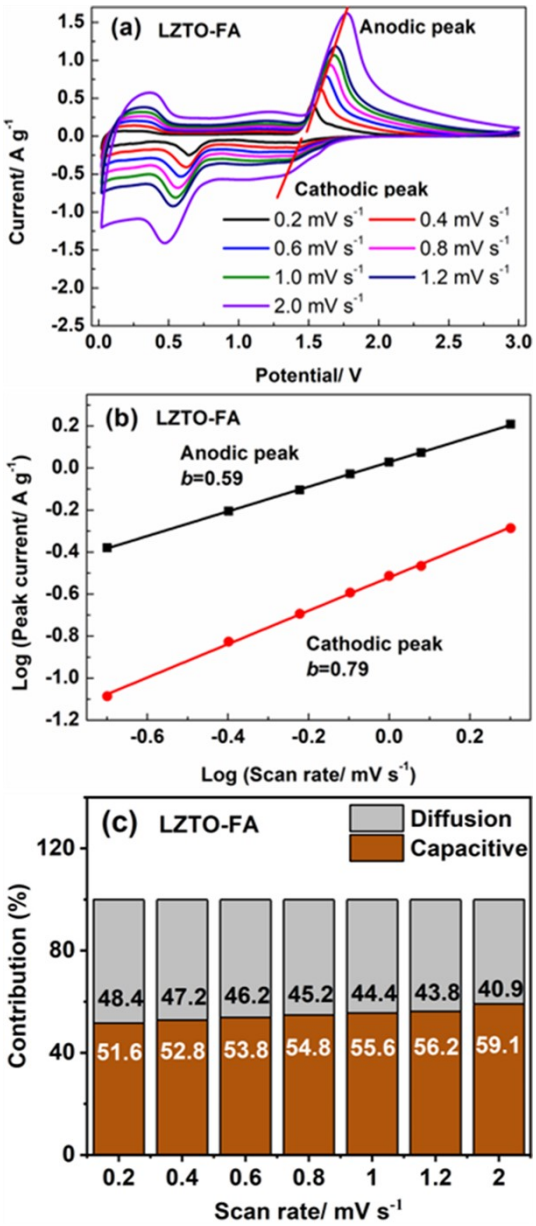

Fig. S8 (a) CV curves of LZTO-FA at different scan rates from 0.2 to 2.0 mV s^{-1}, (b) corresponding log *i* versus log *v* plots at redox peaks (peak current: *i*, scan rate: *v*) and (c) contribution of the pseudocapacitive behaviors of LZTO-FA at different scan rates.

To further understand the kinetic behaviors of Li-storage for LZTO-FA, the CV curves were recorded at different scan rates from 0.2 to 2.0 mV s^{-1} as displayed in Fig. S8a. The peak intensities gradually increase with the increase of the scan rates. In general, the charge-storage type is composed of faradaic intercalation (ion diffusion)

and non-Faradaic (pseudocapacitive) behavior and can be determined by analyzing the relationship between scan rate (v) and peak current (i) based on the equations S4 and S5:

$$i = av^b \tag{S4}$$

$$\log i = b \times \log v + \log a \tag{S5}$$

where a and b are adjustment parameters. b can be obtained by the slope of log i vs. log v. When b values are equal to 0.5 and 1.0, the electrochemical reaction can be controlled by ion diffusion and pseudocapacitance [49], respectively. The b values of the redox peaks for LZTO-FA vary between 0.5 and 1.0, indicating that the coexistence of both the diffusive and capacitive processes (Fig. S8b).

The contribution proportions of the pseudocapacitance (k_1v) and intercalation ($k_2v^{1/2}$) behaviors at different scan rates can be quantitatively calculated by the equation S6 [70]:

$$i = k_1v + k_2v^{1/2} \tag{S6}$$

where k_1 and k_2 represent the contribution from the capacitance-controlled and diffusion-controlled processes, respectively. The capacitive contribution increases gradually with the increase of the scan rate from 0.2 to 2.0 mV s^{-1}. It can be seen that the pseudocapacitive charge-storage has the obvious advantage in the whole capacity, indicating good rate capability.

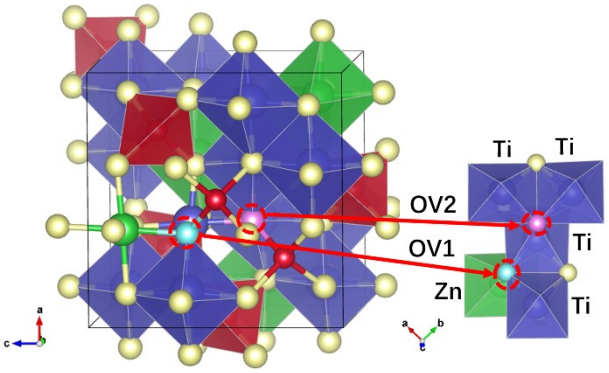

Fig. S9 Possible configurations of oxygen vacancies in *P4₃32* $Li_2ZnTi_3O_8$.

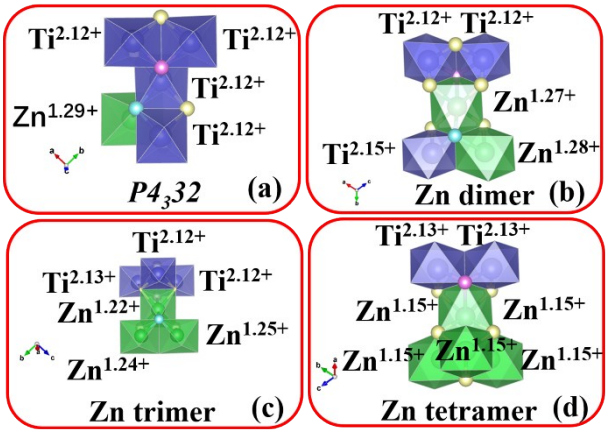

Fig. S10 Local atomic structures of (a) *P4₃32* phase and (b-d) Zn aggregated supercells.

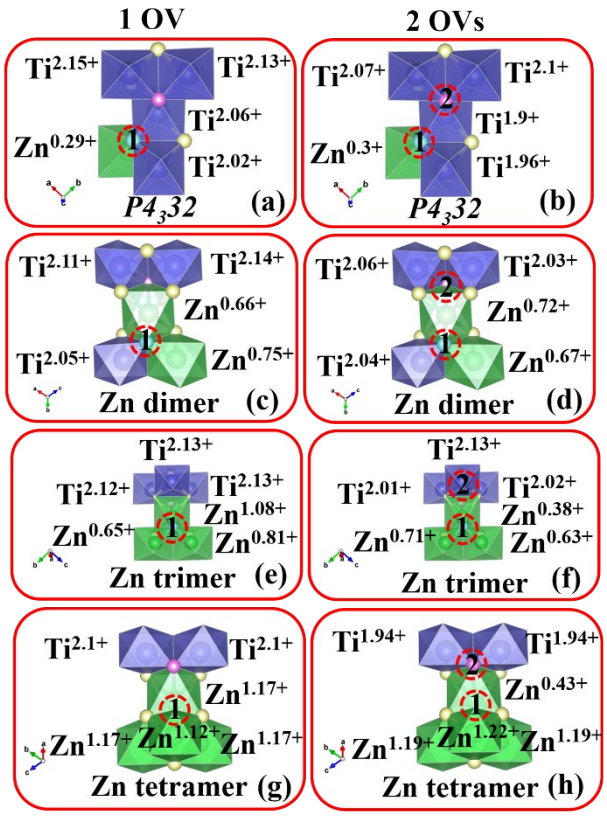

Fig. S11 Local atomic structures of the most energetically favorable OVs in Zn aggregated supercells.

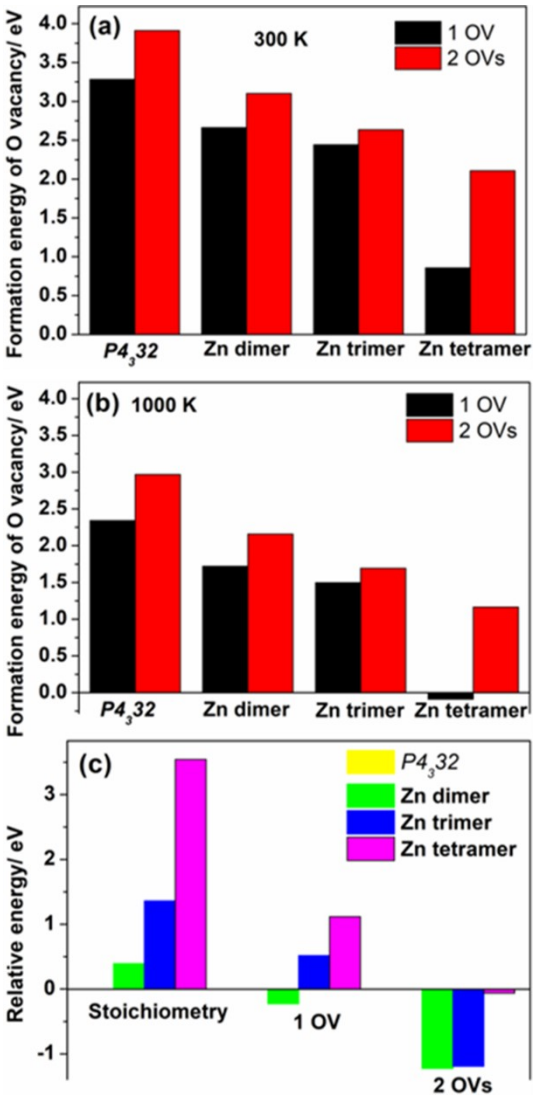

Fig. S12 Formation energies of one or two OVs in *P4₃32* and Zn aggregated supercells at (a) 300 K and (b) 1000 K. (b) Total energies of Zn aggregated supercells relative to the *P4₃32* phase (Total energies of Zn/Ti ordered supercells are set to 0 eV).

Table S10 Equilibrium lattice parameters and cell volumes obtained by calculations.

Samples	*a* (Å)	*b* (Å)	*c* (Å)	*V* (Å^3)
P4₃32 phase	8.3310	8.3310	8.3310	578.2323
LZTO with 1 OV	8.3281	8.3210	8.3584	579.2283
LZTO with 2 OVs	8.3574	8.2987	8.3679	580.3714

Table S11 Intercalation potential and band gap.

Samples	Intercalation potential (V)	Band gap (eV)
$P4_332$ phase	1.34	3.2165
LZTO with 1 OV	1.30	1.2547
LZTO with 2 OVs	1.38	0.1989

Ⅲ. References

[1] Z. Zhang, R. Xun, Z. Shen, L. Wang, S. Wang, Z. Meng, Synthesis of Nb-doped $Li_2ZnTi_3O_8$ anode with long cycle life and applications in the $LiMn_2O_4/Li_2ZnTi_3O_8$ full cell, ACS Sustainable Chemistry & Engineering, 8 (2020) 2763-2771.

[2] G. Kresse, J. Hafner, Ab initio molecular dynamics for liquid metals, Physical Review B, 47 (1993) 558-561.

[3] G. Kresse, J. Hafner, Ab initio molecular-dynamics simulation of the liquid-metal -amorphous-semiconductor transition in germanium, Physical Review B, 49 (1994) 14251-14269.

[4] G. Kresse, J. Furthmüller, Efficiency of ab-initio total energy calculations for metals and semiconductors using a plane-wave basis set, Computational Materials Science, 6 (1996) 15-50.

[5] G. Kresse, J. Furthmüller, Efficient iterative schemes for ab initio total-energy calculations using a plane-wave basis set, Physical Review B, 54 (1996) 11169-11186.

[6] G. Kresse, D. Joubert, From ultrasoft pseudopotentials to the projector augmented-wave method, Physical Review B, 59 (1999) 1758-1775.

[7] P. E. Blöchl, Projector augmented-wave method, Physical Review B, 50 (1994) 17953-17979.

[8] J. P. Perdew, K. Burke, M. Ernzerhof, Generalized gradient approximation made simple, Physical Review Letters, 77 (1996) 3865-3868.

[9] V. I. Anisimov, J. Zaanen, O. K. Andersen, Band theory and Mott insulators: Hubbard *U* instead of Stoner *I*, Physical Review B, 44 (1991) 943-954.

[10] G. Henkelman, B.P. Uberuaga, H. Jonsson, A climbing image nudged elastic band method for finding saddle points and minimum energy paths, Journal of Chemical Physics, 113(2000) 9901-9904.

[11] C. Chen, C. Ai, X. Liu, Ti(III) self-doped $Li_2ZnTi_3O_8$ as a superior anode material for Li-ion batteries, Electrochimica Acta, 265 (2018) 448-454.

[12] K. Liang, X. Huang, X. Hong, Y. Liao, Y. Ren, H. Wang, Sulfur and nitrogen-doped $Li_4Ti_5O_{12}$/rGO as an anode material for advanced sodium-ion batteries, Journal of Alloys and Compounds, 857 (2021) 158190-158198.

[13] X. Deng, Z. Wei, C. Cui, Q. Liu, C. Wang, J. Ma, Oxygen-deficient anatase TiO_2@C nanospindles with pseudocapacitive contribution for enhancing lithium storage, Journal of Materials Chemistry A, 6 (2018) 4013-4022.

[14] T.-F. Yi, L.-Y. Qiu, J. Mei, S.-Y. Qi, P. Cui, S.H. Luo, Y.-R. Zhu, Y. Xie, Y.-B. He, Porous spherical NiO@$NiMoO_4$@PPy nanoarchitectures as advanced electrochemical pseudocapacitor materials, Science Bulletin, 65 (2020) 546-556.

[15] T.F. Yi, L.N. Shi, X. Han, F.F. Wang, Y.R. Zhu, Ying Xie, Approaching high-performance lithium storage materials by constructing hierarchical $CoNiO_2$@CeO_2

nanosheets, Energy & Environmental Materials, 4 (2021) 586-595.

[16] Z. Yao, H. Yin, L. Zhou, G. Pan, Y. Wang, X. Xia, J. Wu, X. Wang, J. Tu, Ti^{3+} self-doped $Li_4Ti_5O_{12}$ anchored on N-doped carbon nanofiber arrays for ultrafast lithium-ion storage, Small, 15 (2019) 1905296-1905302.

[17] J. Lee, X. Cui, Facile preparation of Ti^{3+} self-doped TiO_2 microspheres with lichi-like surface through selective etching, Material Letters, 175 (2016) 114-117.

[18] M. Xing, J. Zhang, B. Qiu, B. Tian, M. Anpo, M. Che, A brown mesoporous TiO_{2-x}/MCF composite with an extremely high quantum yield of solar energy photocatalysis for H_2 evolution, Small, 11 (2015) 1920-1929.

[19] T.-F. Yi, J.-Z. Wu, J. Yuan, Y.-R. Zhu, P.-F. Wang, Rapid lithiation and delithiation property of V-doped $Li_2ZnTi_3O_8$ as anode material for lithium-ion battery, ACS Sustainable Chemistry & Engineering, 3 (2015) 3062-3069.

[20] A. Ziarati, A. Badiei, R. Luque, Black hollow TiO_2 nanocubes: Advanced nanoarchitectures for efficient visible light photocatalytic applications, Applied Catalysis B-Environmental, 238 (2018) 177-183.

[20] C. Chen, C. Ai, X. Liu, Y. He, S. Yang, Y. Wu, High performance $Li_2ZnTi_3O_8$@C anode material fabricated by a facile method without an additional carbon source, Journal of Alloys and Compounds, 698 (2017) 692-698.

[22] Y. Ren, P. Lu, X. Huang, J. Ding, H. Wang, Enhanced electrochemical properties of $Li_2ZnTi_3O_8$/C nanocomposite synthesized with phenolic resin as carbon source, Journal of Solid State Electrochemistry, 21 (2017) 125-131.

[23] A. I. Inamdar, A. T. A. Ahmed, H. S. Chavan, Y. Jo, S. Cho, J. Kim, S. M. Pawar,

B. Hou, S. N. Cha, H. Kim, H. Im, Inflfluence of operating temperature on $Li_2ZnTi_3O_8$ anode performance and high-rate charging activity of Li-ion battery, Ceramics International, 44 (2018) 18625-18632.

[24] Z. Li, H. Li, Y. Cui, Z. Du, Y. Ma, C. Ma, Z. Tang, Li_2MoO_4 modified $Li_2ZnTi_3O_8$ as a high property anode material for lithium ion battery, Journal of Alloys and Compounds, 692 (2017) 131-139.

[25] Z. Meng, L. Wang, X. Li, G. Zhang, H. Li, Synthesis of high performance carbon-coated lithium zinc titanate via an EDTA-assisted route, International Journal of Hydrogen Energy, 42 (2017) 2177-2186.

[26] Z. Meng, S. Wang, X. Chen, L. Wang, F. Wang, Synthesis high rate capability N-doped carbon coated on lithium zinc titanate via a surfacant-assisted solid-state, RSC Advances, 7 (2017) 54258-54265.

[27] Z. Meng, S. Wang, L. Wang, H. Hou, Synthesis of high performance N-doped carbon coated $Li_2ZnTi_3O_8$ via a NTA-assisted solid-state route, Dalton Transactions, 47 (2018) 2711-2718.

[28] S. Wang, L. Wang, Z. Meng, B. Luo, $Li_2ZnTi_3O_8$/graphene nanocomposite as a high-performance anode material for lithium-ion batteries, RSC Advances, 8 (2018) 31628-31632.

[29] S. Wang, L. Wang, Z. Meng, R. Xun, Design of a three-dimensional-network $Li_2ZnTi_3O_8$ co-modified with graphene nanosheets and carbon nanotubes as a high performance anode material for lithium-ion batteries, Journal of Alloys and Compounds, 774 (2019) 581-585.

[30] S. Wang, Y. Bi, L. Wang, Z. Meng, B. Luo, Mo-doped $Li_2ZnTi_3O_8$@graphene as a high performance anode material for lithium-ion batteries, Electrochimica Acta, 301 (2019) 319-324.

[31] Z. Meng, S. Wang, H. Wang, L. Wang, S. Wang, La_2O_3-coated $Li_2ZnTi_3O_8$@C as a high performance anode for lithium-ion batteries, RSC Advances, 9 (2019) 20618-20623.

[32] H. Yang, J. Park, C.S. Kim, Y.H. Xu, H.L. Zhu, Y.X. Qi, L. Yin, H. Li, N. Lun, Y.J. Bai, Uniform surface modification of $Li_2ZnTi_3O_8$ by liquated Na_2MoO_4 to boost electrochemical performance, ACS Appllied Materials & Interfaces, 9 (2017) 43603-43613.

[33] H. Tang, C. Chen, T. Liu, Z. Tang, Chitosan and chitosan oligosaccharide: Advanced carbon sources are used for preparation of N-doped carbon-coated $Li_2ZnTi_3O_8$ anode material, Journal of Electroanalytical Chemistry, 858 (2020) 113789-113797.

[34] Z. Shen, Z. Zhang, S. Wang, Z. Liu, L. Wang, Y. Bi, Z. Meng, Mg^{2+}–W^{6+} co-doped $Li_2ZnTi_3O_8$ anode with outstanding room, high and low temperature electrochemical performance for lithium-ion batteries, Inorganic Chemistry Frontiers, 6 (2019) 3288-3294.

[35] H. Li, Z. Li, Y. Cui, C. Ma, Z. Tang, Long-cycled $Li_2ZnTi_3O_8/TiO_2$ composite anode material synthesized via a one-pot co-precipitation method for lithium ion batteries, New Journal of Chemistry, 41 (2017) 975-981.

[36] S. Yıldız, H. Şahan, In situ synthesis of reduced graphite oxide-$Li_2ZnTi_3O_8$

composite as a high rate anode material for lithium-ion batteries, Journal of The Electrochemical Society, 166 (2019) A2002-A2012.

[37] N. Firdous, N. Arshad, P. Norby, Synergic effect of niobium doping and carbon coating on the performance of a $Li_2ZnTi_3O_8$ anode candidate for lithium ion batteries, Energy & Fuels, 34 (2020) 14968-14974.

[38] N. Firdous, N. Arshad, S.B. Simonsen, P. Kadirvelayutham, P. Norby, Advanced electrochemical investigations of niobium modified $Li_2ZnTi_3O_8$ lithium ion battery anode materials, Journal of Power Sources, 462 (2020) 228186-228195.

[39] T. Lan, L. Chen, Y. Liu, W. Zhang, M. Wei, Nanocomposite $Li_2ZnTi_3O_8$/C with enhanced electrochemical performances for lithium-ion batteries, Journal of Electroanalytical Chemistry, 794 (2017) 120-125.

[40] H. Yang, X.-H. Wang, Y.-X. Qi, N. Lun, Y.-M. Cao, Y.-J. Bai, Improving the electrochemical performance of $Li_2ZnTi_3O_8$ by surface KCl modification, ACS Sustainable Chemistry & Engineering, 5 (2017) 6099-6106.

[41] H. Yang, N. Lun, Y.-X. Qi, H.-L. Zhu, J.-R. Liu, J.-K. Feng, L.-l. Zhao, Y.-J. Bai, $Li_2ZnTi_3O_8$ coated with uniform lithium magnesium silicate layer revealing enhanced rate capability as anode material for Li-ion battery, Electrochimica Acta, 315 (2019) 24-32.

[42] J.-L. Qin, H.-L. Zhu, N. Lun, Y.-X. Qi, Y.-J. Bai, $Li_2ZnTi_3O_8$/C anode with high initial Coulombic efficiency, long cyclic life and outstanding rate properties enabled by fulvic acid, Carbon, 163 (2020) 297-307.

[43] H. Yang, J. Park, C.-S. Kim, Y.-H. Xu, H.-L. Zhu, Y.-X. Qi, L.-W. Yin, H. Li,

N. Lun, Y.-J. Bai, Boosted electrochemical performance of $Li_2ZnTi_3O_8$ enabled by ion-conductive Li_2ZrO_3 concomitant with superficial Zr-doping, Journal of Power Sources, 379 (2018) 270-277.

[44] H. Yang, H.-L. Zhu, Y.-X. Qi, N. Lun, Y.-J. Bai, Optimizing the cycling life and high-rate performance of $Li_2ZnTi_3O_8$ by forming thin uniform carbon coating derived from citric acid, Journal of Materials Science, 55 (2020) 15538-15550.

[45] X. Zeng, J. Peng, H. Zhu, Y. Gong, X. Huang, Cr-doped $Li_2ZnTi_3O_8$ as a high performance anode material for lithium-ion batteries, Frontiers in Chemistry, 8 (2020) 600204-600210.

[46] H. Tang, T. Liu, Z. Tang, The stereo-microstructure of ZnO affects the lithium storage capacity of $Li_2ZnTi_3O_8$ anode materials, Dalton Transactions, 48 (2019) 12303-12314.

[47] H. Tang, Y. Song, L. Zan, Y. Yue, D. Dou, Y. Song, M. Wang, X. Liu, T. Liu, Z. Tang, Characterization of lithium zinc titanate doped with metal ions as anode materials for lithium ion batteries, Dalton Transactions, 50 (2021) 3356-3368.

[48] Y. Li, T.-F. Yi, X. Li, X. Lai, J. Pan, P. Cui, Y.-R. Zhu, Y. Xie, $Li_2ZnTi_3O_8$@α-Fe_2O_3 composite anode material for Li-ion batteries, Ceramics International, 47 (2021) 18732-18742.

[49] L. Qiu, X.-Q. Lai, F. Wang, J. Pan, Y.-R. Zhu, P. Cui, T.-F. Yi, Promoting the Li storage performances of $Li_2ZnTi_3O_8$@Na_2WO_4 composite anode for Li-ion battery, Ceramics International, 47 (2021) 19455-19463.

[50] Q. He, Z.G. Sun, X.W. Shi, W.W. Wu, J.P. Cheng, R.F. Zhuo, Z.Y. Zhang, J.

Wang, Electrochemical performance enhancement of nitrogen-doped TiO_2 for lithium-ion batteries investigated by a film electrode model, Energy & fuels, 35 (2021) 2717-2726.

[51] X.M. Lu, F.Y. Luo, Q.H. Tian, W. Zhang, Z.Y. Sui, J.Z. Chen, Anatase TiO_2 nanowires intertangled with CNT for conductive additive-free lithium-ion battery anodes, Journal of Physics and Chemistry of Solids, 153 (2021) 110037-110043.

[52] T. Partheeban, T. Kesavan, A. Jithin, S. Dharaneshwar, M. Sasidharan, Melamine-templated TiO_2 nanoparticles as anode with high capacity and cycling stability for lithium-ion batteries, Journal of Solid State Electrochemistry, 25 (2021) 919-926.

[53] Y. Wang, N. Li, C. Hou, B. He, J. Li, F. Dang, J. Wang, Y. Fan, Nanowires embedded porous TiO_2@C nanocomposite anodes for enhanced stable lithium and sodium ion battery performance, Ceramics International, 46 (2020) 9119-9128.

[54] X. Shen, M. Chen, X. Hong, W. Wang, Z. Qiao, J. Chen, S. Fan, J. Yu, C. Tang, Synthesis and anodic performance of TiO_2-carbonized PAN electrode for lithium ion batteries, Chemical Physics, 530 (2020) 110639-110643.

[55] Y. Zhang, M. Zhang, Y. Liu, H. Zhu, L. Wang, Y. Liu, M. Xue, B. Li, X. Tao, Oxygen vacancy regulated $TiNb_2O_7$ compound with enhanced electrochemical performance used as anode material in Li-ion batteries, Electrochimica Acta, 330 (2020) 135299-135308.

[56] J. Luo, J. Peng, P. Zeng, Z. Wu, J. Li, W. Li, Y. Huang, B. Chang, X. Wang, $TiNb_2O_7$ nano-particle decorated carbon cloth as flexible self-support anode material

in lithium-ion batteries, Electrochimica Acta, 332 (2020) 135469-135479.

[57] Ö. Budak, P. Srimuk, M. Aslan, H. Shim, L. Borchardt, V. Presser, Titanium niobium oxide $Ti_2Nb_{10}O_{29}$/carbon hybrid electrodes derived by mechanochemically synthesized carbide for high-performance lithium-ion batteries, ChemSusChem, 14 (2021) 398-407.

[58] C.-H. Lu, K.-C. Li, S. Balaji, P.S. Kumar, Agar-assisted sol-gel synthesis and electrochemical characterization of $TiNb_2O_7$ anode materials for lithium-ion batteries, Ceramics International, 47 (2021) 18619-18624.

[59] R.F. Qian, C.F. Yang, D.W. Ma, K.M. Li, T. Feng, J.J. Feng, J. H. Pan, Robust lithium storage of block copolymer-templated mesoporous $TiNb_2O_7$ and $TiNb_2O_7$@C anodes evaluated in half-cell and full-battery configurations, Electrochimica Acta, 379 (2021) 138179-138189.

[60] C.H. Wang, L. Huang, Y. Zhong, X.L. Tong, C.D. Gu, X.H. Xia, Lingjie Zhang, X.L. Wang, J.P. Tu, $Ti_2Nb_{10}O_{29}$ anchored on Aspergillus Oryzae spore carbon skeleton for advanced lithium ion storage, Sustainable Materials and Technologies, 28 (2021) e00272.

[62] H.B. Ding, Z.H. Song, K. Feng, H.Z. Zhang, H.M. Zhang, X.F. Li, Controlled synthesis of pure-phase metastable tetragonal Nb_2O_5 anode material for high-performance lithium batteries, Journal of Solid State Chemistry, 299 (2021) 122136-122143.

[63] N. Li, X.W. Lan, L.B. Wang, Y.J. Jiang, S.T. Guo, Y.Q. Li, X.L. Hu, Precisely tunable T-Nb_2O_5 nanotubes via atomic layer deposition for fast-charging lithium-ion

batteries, ACS Applied Materials & Interfaces, 13 (2021) 16445-16453.

[64] X.M. Zhang, J.Y. Wang, X.B. Wang, Y.B. Li, Y. Zhao, Z. Bakenov, G. Li, 3D ordered macroporous amorphous Nb_2O_5 as anode material for high-performance sodium-ion batteries, Applied Surface Science, 567 (2021) 150862-150870.

[65] Y. Lian, Y.J. Zheng, Y.Q. Bai, D.W. Wang, H.S. Yan, Z.F. Wang, J. Zhao, H.H. Zhang, Oxygen defected T-Nb_2O_{5-x} confined in necklace-like N-doped carbon fibers for Li^+/Na^+ capacitor, Journal of Power Sources, 507 (2021) 230267-230276.

[66] P.P. Jing, K.T. Liu, L. Soule, J. Wang, T.T. Li, B. Zhao, M.L. Liu, Engineering the architecture and oxygen deficiency of *T*-Nb_2O_5-carbon-graphene composite for high-rate lithium-ion batteries, Nano Energy, 89 (2021) 106398-106407.

[67] T. Yang, Z.Z. Yang, X.F. Cheng, Y.H. Ding, Y.X. Fan, G.X. Liu, K. Zhang, S.Y. Jin, X.D. Liu, Z.P. Qiao, Three-dimensional hierarchical urchin-like Nb_2O_5 microspheres wrapped with N-doped carbon: An advanced anode for lithium-ion batteries, Journal of Alloys and Compounds, 876 (2021) 160145-160154.

[68] W. Liu, X. Zhang, C. Li, K. Wang, X. Sun, Y. Ma, Carbon-coated Li_3VO_4 with optimized structure as high capacity anode material for lithium-ion capacitors, Chinese Chemical Letters, 31 (2020) 2225-2229.

[69] N. Gautam, R. Muhammad, H. Raj, A. Sil, P. Mohanty, T.K. Mandal, Multimodal mesopore hierarchy in Li_3VO_4 boosts electrochemical anode performance of lithium-ion batteries, Microporous and Mesoporous Materials, 290 (2019) 109669-109673.

[70] Y. Wang, H.T. Shi, J.R. Niu, W. Mai, L.Y. Liu, Z.W. Xu, Self-healing

Sn_4P_3@hard carbon co-storage anode for sodium-ion batteries, Journal of Alloys Compounds, 851 (2021) 156746-156755.